JOURNAL OF SPACECRAFT AND ROCKETS
Vol. 45, No. 5, September–October 2008

# Improved Atomic Oxygen Quantification Within the Earth's Upper Atmosphere Through Numerical Corrections

Jeffrey Allen* and Thomas Hauser†
*Utah State University, Logan, Utah 84322*

DOI: 10.2514/1.31924

**An established method to simulate the aerodynamic effects on in situ sounding rocket measurements is the direct simulation Monte Carlo method. However, very few three-dimensional steady and unsteady simulations with high resolution along a rocket trajectory exist. This study provides three-dimensional steady and unsteady simulations applied to the Second Coupling of Dynamics and Aurora experiment. The results show the validity of a steady-state approach through quantitative comparisons of steady and unsteady simulation results near the rocket's apogee. Steady-state solutions of the flowfield are presented at 2 km intervals along both the upleg and downleg trajectories. The numerical simulations verify the experimental results showing the strong influence of rocket orientation on concentration. Atomic oxygen correction factors, based on the ratio of undisturbed to disturbed flowfield concentrations, are obtained from the numerical results and applied to the experimental sensor data. These correction factors, when applied to uncorrected Second Coupling of Dynamics and Aurora data sets, show a significant improvement over previous research results, particularly along the upleg trajectory, in terms of minimizing the effects of compressible flow aerodynamics on the atomic oxygen data.**

## Nomenclature

| | | |
|---|---|---|
| $\langle c \rangle$ | = | molecular speed |
| $H$ | = | altitude, km |
| $Kn$ | = | Knudsen number based on the mean free path in the atmosphere and the rocket diameter as the reference length |
| $M$ | = | Mach number |
| $N_2$ | = | molecular nitrogen |
| $n$ | = | number density, $1/m^3$ |
| O | = | atomic oxygen |
| $O_2$ | = | molecular oxygen |
| $O_3$ | = | ozone |
| $T$ | = | temperature, K |
| $V$ | = | rocket velocity, m/s |
| $\alpha$ | = | angle of attack, deg |
| $\Delta t$ | = | global time step |
| $\delta$ | = | grid cell volume |
| $\lambda$ | = | mean free path |

*Subscripts*

| | | |
|---|---|---|
| $i$ | = | cell index |
| mean | = | average value |
| $S$ | = | surface condition of the sounding rocket |
| $\infty$ | = | undisturbed atmospheric or inflow conditions |

## I. Introduction

THE study of atomic oxygen concentrations within the Earth's mesosphere and lower thermosphere is among the principle interests of atmospheric scientists. The correct assessment of atomic oxygen concentrations in the mesosphere and lower thermosphere is important for several reasons, including: the creation of ozone $O_3$, the expansion and contraction of the atmosphere, and global climate change [1]. Among the various means of measuring atomic oxygen concentrations in the mesosphere and lower thermosphere, in situ measurements using sensor platforms aboard sounding rockets have proven very useful in providing an enhanced understanding and quantification of atomic oxygen concentrations. Unfortunately, however, significant discrepancies continue to exist between these measured data and other atmospheric models such as the U.S. standard atmosphere, the Jacchia reference atmosphere, and the 2000 version of the Mass Spectrometer Incoherent Scatter Radar Extended (MSISE-00) model [2]. Perhaps more alarming, however, is the *inconsistency in localized experiments* to adequately describe a uniform quantification of atomic oxygen. This inconsistency is brought about as a result of the compressible flow aerodynamics, and more specifically, the position/orientation of the atomic oxygen sensor with respect to the external flowfield.

The first numerical simulation of the aerodynamic effects of a sounding rocket on measurements using the direct simulation Monte Carlo (DSMC) method was performed by Bird [3]. Other studies [4–8] used the DSMC method for the analysis of in situ measurements for a wide variety of measurement techniques. An earlier DSMC study [9] of the Second Coupling of Dynamics and Aurora (CODA II) mission showed that it is possible to analyze the aerodynamic influence of the flowfield on the sensor data by numerically simulating the CODA II payload at various points along its trajectory. Atomic oxygen concentration results from these simulations were then used to compute correction functions based on the ratio of undisturbed to disturbed concentrations. These correction functions were then applied directly to the experimental data sets and resulted in significant improvement. The results from this early study, however, were limited to a small number of locations along the trajectory because of excessive compute times on a single workstation required for each case.

In this study a new and parallelized implementation of the DSMC method, foamDSMC [10], is used to provide three-dimensional, high-resolution, steady and unsteady flow fields of the CODA II mission. The parallel solver is used to simulate unsteady flowfields near the apogee of the trajectory, where the angle of attack $\alpha$ changes most dramatically, and where the mean free path $\lambda$ is sufficiently large. Steady-state flowfield simulations are conducted at 2 km intervals along the trajectory. The results show that there is no substantial difference between the steady and unsteady results. Job

Presented as Paper 610 at the 45th AIAA Aerospace Sciences Meeting and Exhibit, Reno, NV, 8–11 January 2007; received 3 May 2007; revision received 10 September 2007; accepted for publication 14 September 2007. 

*Mechanical Engineer, Engineering Research and Development Center, U.S. Army Corps of Engineers. Member AIAA.

†Assistant Professor, Mechanical and Aerospace Engineering Department. Associate Fellow AIAA.

level parallelism [11] enables the fast completion of many realizations along the trajectory, whereas domain decomposition techniques [12] overcome the large compute times for a single simulation associated with the large number of particles necessary to resolve the small mean free path in low altitudes. The steady flow solutions along the trajectory are then used to correct the measured atomic oxygen data for the orientational influence of the flowfield using the correction function approach [8].

## II. Problem Definition

### A. CODA II and ATOX Sensor Geometry

The CODA II sounding rocket experiment, sponsored by NASA, was launched to observe the effects of an active aurora on the neutral atmosphere. CODA II was launched 21 February 2002 at 09:55 UT (00:55 local) and reached an apogee of 139.74 km. The flight was launched aboard a Black Brant VC rocket and originated from the University of Alaska's Poker Flat Research Range (65° north latitude, 147° west longitude). The payload maintained a constant rotational frequency about its longitudinal axis of $H = 1$, and a constant pitch angle of 60.9 deg. The payload consisted of several sensors, including one developed by Utah State University called ATOX [13]. The ATOX sensor was used to measure atomic oxygen concentrations and is based on the resonant fluorescence/absorption technique [2]. In addition, the CODA II mission contained several photometers, a neutral mass spectrometer, an ionization gauge, a direct current capacitance probe, and a plasma frequency probe [2].

Figure 1a shows the geometry of the Black Brant VC rocket after the nose cone was ejected. The reference point for the geometry is the nose section of geometry. As indicated in Fig. 1a, the ATOX booms are located approximately 2.76 m aft of the nose section, and extend approximately 0.5 m and 0.33 m on opposite sides of the fuselage. Figure 1b shows the sensor field of view from the side. The absorption photometer sits at the end of the ATOX boom assembly and is looking back toward the rocket's fuselage. The resonance fluorescence sensors are located approximately 0.13 m forward of the booms and are integrated into the rocket and are inclined at 45 deg to the fuselage wall, as shown in Fig. 1b.

The resonance fluorescence sensors scan a measurement volume of $12.6 \times 10^{-3}$ sr (sr is an SI unit of solid angle) which, when intersected with the $22.36 \times 10^{-3}$ sr volume of the vacuum ultraviolet lamps, constitutes the ATOX sensor field of view. The resonant fluorescence/absorption technique, which has been used both in the laboratory and the atmosphere, relies on the output of the 130-nm triplet from atomic line sources (lamps) to initiate the measurement [13]. The lamps electronically excite internal oxygen atoms that emit the vacuum ultraviolet triplet as sources within the rocket payload [14,15]. As depicted in Fig. 1b, the emitted radiation is broadcast over a small volume surrounding the payload. Boom mounted photometers measure the radiated energy that passes through the volume unabsorbed, whereas payload-mounted photometers monitor the small portion of energy that is absorbed and reradiated by atomic oxygen within the measurement volume [16]. The absorption and resonant fluorescence measurements are complementary. The resonant fluorescence photometers provide a highly sensitive concentration measurement of the region, whereas the absorption photometers provide a direct calibration throughout the flight [14,17]. Using outputs from both resonant fluorescence and absorption photometry make it possible to ascertain the concentration of atomic oxygen within the sensor field of view.

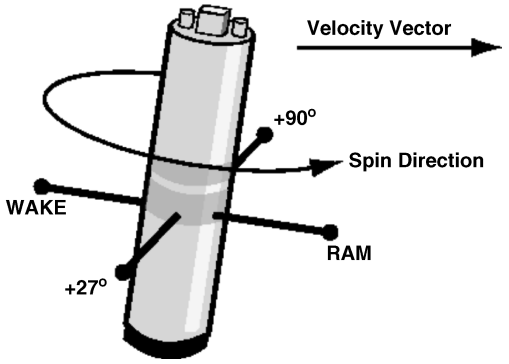


**Fig. 2 Definition of ram, wake, and cross-track sensor orientation with respect to the horizontal rocket velocity component.**

The orientation of the sensors is referenced with respect to the long ATOX boom. Three orientations are defined by the orientation of this boom with respect to the horizontal velocity of the sounding rocket as shown in Fig. 2.

RAM is the long ATOX boom, oriented in the direction of the horizontal velocity of the sounding rocket.

CROSS TRACK is the long ATOX boom, oriented 90 or 270 deg from the ram direction.

WAKE is the long ATOX boom, oriented 180 deg from the ram direction.

### B. CODA II Atomic Oxygen Data

Normalized atomic oxygen data (upleg and downleg) from the CODA II (NAG5-5187) mission, is shown in Fig. 3. Normalization is based on the maximum atomic oxygen density. This figure shows that the atomic oxygen concentration is not only strongly dependent on the altitude but also on the sensor orientation. The difference between the three atomic oxygen concentration curves for the upleg and the corresponding three for the downleg, is clearly created by the highly asymmetric flowfield around the sounding rocket. The upleg ram to wake and ram to cross-track ratios at 90 km are approximately 6.5 and 1.3, respectively. The downleg ram to wake and ram to cross-track ratios at 105 km are approximately 6.7 and 1.3, respectively.

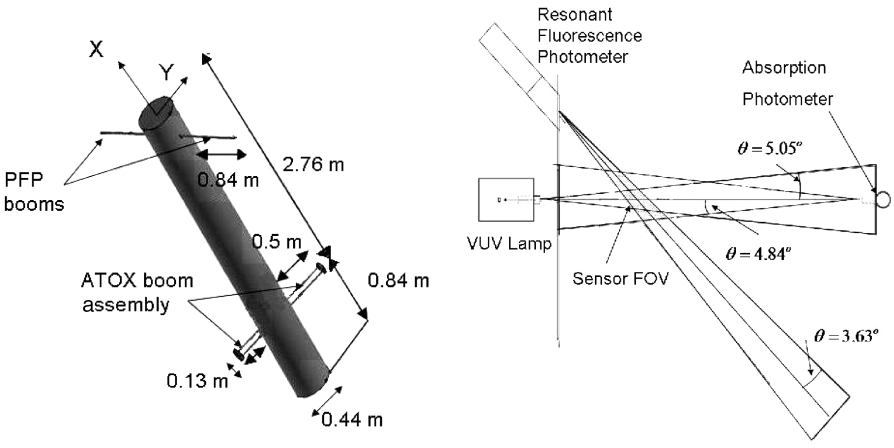


**a) CODA II geometry** **b) ATOX sensor configuration**

**Fig. 1 CODA II geometry, the USU ATOX sensor, and the orientation reference.**

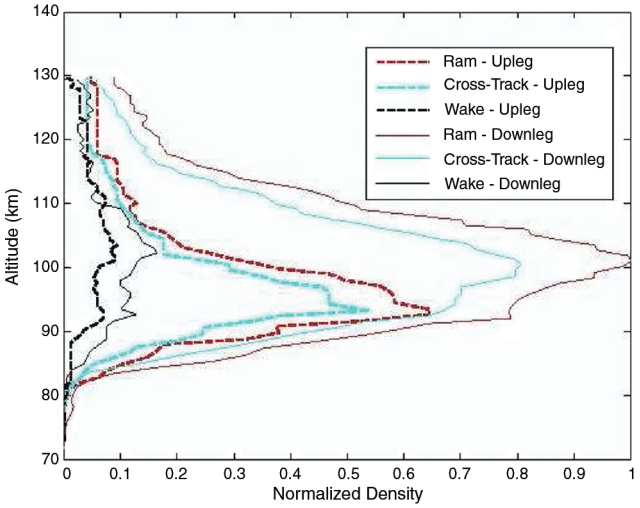


**Fig. 3 Uncorrected experimental atomic oxygen sensor data from CODA II, showing the effects of rocket orientation and trajectory.**

This demonstrates the need to correct the atomic oxygen concentration for the aerodynamic influences.

## III. Direct Simulation Monte Carlo Method

The steady and unsteady DSMC method is applied to simulate the steady and unsteady flow around the rocket. Details of the DSMC method are described in Bird [18]. Implementation, parallelization, and validation of the foamDSMC code is detailed in Allen and Hauser [10]. The DSMC method is a direct simulation method based on kinetic theory and may be regarded as a numerical solution to the Boltzmann equation in the limit of very large numbers of simulated molecules [19,20]. The method, as its name implies, may be categorized as a Monte Carlo method in that it makes extensive use of random numbers to help in the stochastic generation of continuum variables. The primary objective of the method is to approximate these variables by means of modeling the interactions of a statistically significant number of simulated molecules, each representing a much larger subset of the real, unmodeled gas. The deterministic motions and probabilistic collisions of these simulated molecules are modified over sufficiently small time steps, which are governed by the mean collision frequency. Because the tracking and molecular interactions are conducted on a particle by particle basis, the conservation of mass, momentum, and energy may be enforced to machine accuracy [21].

For the simulation results presented in this study, the rocket was approximated by a simple cylinder, and the computational domain is discretized by an unstructured tetrahedral mesh. Examples of this mesh can be seen in Fig. 4. For the parallel computations, the unstructured, hexagonal, or tetrahedral mesh is distributed through domain decomposition among the desired number of processors. Input flow and species conditions appropriate to either steady state or unsteady applications are set, as well as a reasonable small time step, set in accordance with the mean collision time. The time step $\Delta t$ is computed based on the requirement that the mean distance traveled by a particle is less than the mean free path

$$\Delta t = \frac{1}{4} \cdot \frac{\min(\sqrt[3]{\delta_i})}{\langle c \rangle_{\text{mean}}} \tag{1}$$

where $\sqrt[3]{\delta_i}$ is a measure for the cell width and $\langle c \rangle_{\text{mean}}$ is the mean molecular speed. This assignment of $\Delta t$ is justified by the fact that the largest cell widths were no greater than a single mean free path, regardless of altitude, and, in most cases, substantially less.

The core DSMC routines including particle initialization, movement, boundary interactions, collisions, and sampling are then executed in accordance with Bird [18], with interprocessor communication occurring only when particles transfer from one processor boundary to another. In its present state, the foamDSMC solver allows accommodation only for variable hard sphere (VHS) molecules [18] and exclusively assumes diffuse boundary interactions with complete thermal accommodation to surface temperatures. Vibrational energy models are not included in the current implementation. Unsteady and steady-state simulation runs are conducted via ensemble averaging and time averaging, respectively.

It will be shown, that the unsteady results conducted near apogee (see Sec. III.B) do not deviate appreciably from the corresponding steady-state results. This, therefore, precluded the need for unsteady simulations at or near apogee. Because the apogee and near-apogee altitude regions constitute the largest changes compared with the lower altitudes in terms of both rarefaction and angle of attack (see Table 1), these findings were generalized, and steady-state simulations were deemed appropriate over the entire CODA II trajectory.

### A. Steady-State Results

The steady-state solver was applied to 25 different altitudes, each separated by 2 km intervals, along both the up- and downleg trajectory, for a total of 49 separate simulations. Table 1 summarizes the inflow conditions for all the steady simulations along the trajectory. The bold numbers in this table show the values for the downleg portion of the trajectory. The values for the number density $n$ and the fractions of atomic oxygen O, molecular oxygen $O_2$, and nitrogen $N_2$, as well as the inflow temperature $T_\infty$, were obtained from the MSISE-00 [22] model. The surface temperature of the sounding rocket $T_S$, velocity $|V|$, and angle of attach $\alpha$ were obtained from the sounding rocket flight data. The Knudsen number $Kn$ is based on the mean free path $\lambda_\infty$ in the atmosphere and the diameter of the rocket as the reference length.

#### 1. *Inflow Conditions and Grids*

Several different grids were required, each with varying cell sizes proportional to the mean free path, as shown in Table 1. As a general rule, a different grid was required for each 10 km interval. Figure 4a–4c shows a cross-sectional cut of representative grids corresponding to altitudes of 90 km, 110 km, and apogee, respectively.

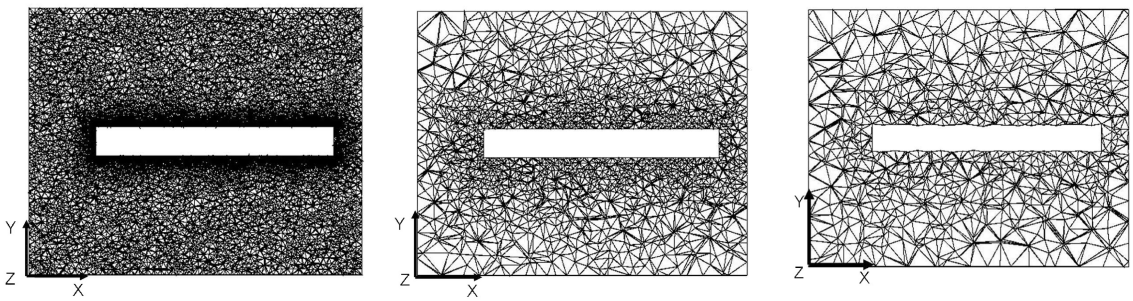


**a) 90 km** **b) 100 km** **c) Apogee**

**Fig. 4 Representative SMC grid cross sections corresponding to 90 km, 110 km, and apogee, taken at the $z$-coordinate midplane.**

**Table 1 Initial conditions for steady-state SMC simulations (bold numbers are for the downleg of the trajectory)**

| $H$, km | $n$, m$^{-3}$ | Frac O | Frac $O_2$ | Frac. $N_2$ | $T_\infty$, K | $T_s$, K | $\|V\|$, m/s | $\alpha$, deg | $\lambda_\infty$, m | $M$ | $Kn$ |
|---|---|---|---|---|---|---|---|---|---|---|---|
| 90 | 5.61E + 19 | 3.47E − 03 | 2.06E − 01 | 7.91E − 01 | 194.7 | 356.15/**379.15** | 1276.87 | 11.69/**110.10** | 0.02 | 4.13 | 0.04 |
| 92 | 4.06E + 19 | 6.79E − 03 | 2.03E − 01 | 7.90E − 01 | 191.2 | 358.48/**379.15** | 1261.42 | 12.29/**109.54** | 0.03 | 4.12 | 0.06 |
| 94 | 2.91E + 19 | 1.19E − 02 | 2.00E − 01 | 7.88E − 01 | 188.2 | 360.82/**379.15** | 1245.78 | 12.93/**108.98** | 0.04 | 4.1 | 0.08 |
| 96 | 2.07E + 19 | 1.90E − 02 | 1.96E − 01 | 7.85E − 01 | 186.3 | 363.15/**379.15** | 1229.94 | 13.6/**108.43** | 0.05 | 4.07 | 0.12 |
| 98 | 1.46E + 19 | 2.81E − 02 | 1.91E − 01 | 7.81E − 01 | 186.2 | 364.15/**379.15** | 1213.44 | 14.32/**107.88** | 0.07 | 4.02 | 0.17 |
| 100 | 1.02E + 19 | 3.90E − 02 | 1.85E − 01 | 7.76E − 01 | 188.6 | 365.15/**379.15** | 1197.64 | 15.04/**106.99** | 0.1 | 3.94 | 0.24 |
| 102 | 7.08E + 18 | 5.18E − 02 | 1.77E − 01 | 7.71E − 01 | 194.1 | 366.15/**379.48** | 1181.15 | 15.82/**106.14** | 0.15 | 3.83 | 0.34 |
| 104 | 4.91E + 18 | 6.61E − 02 | 1.69E − 01 | 7.65E − 01 | 202.9 | 367.15/**379.82** | 1164.48 | 16.64/**105.61** | 0.22 | 3.69 | 0.5 |
| 106 | 3.42E + 18 | 8.18E − 02 | 1.60E − 01 | 7.58E − 01 | 214.9 | 368.15/**380.15** | 1147.48 | 17.52/**104.39** | 0.32 | 3.53 | 0.72 |
| 108 | 2.40E + 18 | 9.85E − 02 | 1.51E − 01 | 7.51E − 01 | 230.3 | 369.65/**380.65** | 1130.76 | 18.42/**103.54** | 0.46 | 3.36 | 1.04 |
| 110 | 1.71E + 18 | 1.16E − 01 | 1.41E − 01 | 7.43E − 01 | 249.1 | 371.15/**381.15** | 1112.79 | 19.44/**102.65** | 0.65 | 3.18 | 1.48 |
| 112 | 1.24E + 18 | 1.34E − 01 | 1.32E − 01 | 7.35E − 01 | 271.3 | 371.82/**381.48** | 1095.04 | 20.5/**101.41** | 0.91 | 3 | 2.08 |
| 114 | 9.11E + 17 | 1.51E − 01 | 1.23E − 01 | 7.26E − 01 | 297.1 | 372.48/**381.82** | 1076.99 | 21.64/**100.16** | 1.26 | 2.82 | 2.87 |
| 116 | 6.83E + 17 | 1.69E − 01 | 1.15E − 01 | 7.17E − 01 | 326.4 | 373.15/**382.15** | 1058.64 | 22.87/**98.92** | 1.71 | 2.65 | 3.89 |
| 118 | 5.21E + 17 | 1.85E − 01 | 1.07E − 01 | 7.08E − 01 | 358.8 | 373.65/**382.65** | 1039.97 | 24.2/**97.70** | 2.28 | 2.48 | 5.19 |
| 120 | 4.06E + 17 | 2.01E − 01 | 1.00E − 01 | 6.99E − 01 | 393.3 | 374.15/**383.15** | 1020.96 | 25.65/**96.51** | 2.97 | 2.32 | 6.78 |
| 122 | 3.24E + 17 | 2.16E − 01 | 9.43E − 02 | 6.90E − 01 | 427.4 | 374.82/**383.15** | 1001.59 | 27.25/**94.85** | 3.77 | 2.19 | 8.61 |
| 124 | 2.64E + 17 | 2.30E − 01 | 8.91E − 02 | 6.81E − 01 | 458.8 | 375.48/**383.15** | 981.76 | 29.03/**92.95** | 4.68 | 2.07 | 10.69 |
| 126 | 2.20E + 17 | 2.43E − 01 | 8.45E − 02 | 6.72E − 01 | 488.4 | 376.15/**383.15** | 961.59 | 31.01/**90.97** | 5.68 | 1.96 | 12.96 |
| 128 | 1.85E + 17 | 2.56E − 01 | 8.06E − 02 | 6.64E − 01 | 516.6 | 377.15/**383.15** | 941.12 | 33.25/**88.91** | 6.8 | 1.87 | 15.53 |
| 130 | 1.58E + 17 | 2.68E − 01 | 7.70E − 02 | 6.55E − 01 | 543.5 | 378.15/**383.15** | 920.71 | 35.78/**86.21** | 8.02 | 1.78 | 18.32 |
| 132 | 1.36E + 17 | 2.79E − 01 | 7.40E − 02 | 6.47E − 01 | 569.2 | 378.82/**383.15** | 898.58 | 38.97/**83.10** | 9.37 | 1.7 | 21.38 |
| 134 | 1.19E + 17 | 2.90E − 01 | 7.13E − 02 | 6.39E − 01 | 593.7 | 379.48/**383.15** | 877.14 | 42.76/**79.24** | 10.76 | 1.63 | 24.57 |
| 136 | 1.04E + 17 | 3.01E − 01 | 6.88E − 02 | 6.30E − 01 | 617 | 380.15/**383.15** | 853.71 | 48.39/**73.61** | 12.36 | 1.55 | 28.22 |
| 138 | 9.20E + 16 | 3.11E − 01 | 6.65E − 02 | 6.22E − 01 | 639.3 | 381.15 | 833.3 | 60.89 | 14.01 | 1.49 | 31.99 |

The number of cells ranged from over 1.1 million for the lower 90 km altitudes to approximately 3.0 thousand for apogee and near-apogee cases. The number of simulated molecules also varied in accordance with the number of cells. In general, to maintain a statistically significant sample size, the average number of molecules per cell was no less than ten. The proportionality of the grid cells to the mean free path was dependent on the suspected gradients of the flowfield. For undisturbed portions, the cell widths were no more than one mean free path. For suspected regions of large flow gradients the cell widths were initially assigned at one third of the mean free-path length. These were subsequently refined as needed to arrive at grid-independent results.

The number of simulated molecules from 90 km to apogee thus ranged from approximately 11.0 million to 30,000. The freestream flow and species properties shown in Table 1 were obtained from the MSISE-00 [22] atmospheric model (downleg conditions shown in bold), whereas other input conditions, including the species diameter, mass, and viscosity index were obtained from Appendix A of Bird [18]. The macroscopic number density was sampled in all cases every two time steps, whereas output files were written every 300 time steps. The simulations were all conducted in parallel, using Utah State University's Uinta cluster supercomputer, consisting of 256 AMD Opteron 264 1.8 GHz processors. The number of required processors varied in accordance with problem size (as quantified by both the number of cells and the number of simulated molecules) and ranged from 4 to 16 processors. The computational domain was all decomposed in accordance with the *simple* method [23] and was primarily partitioned along the $x$- and $y$-coordinate axes, in accordance with Fig. 1a.

### 2. *Gas Temperatures*

In Fig. 5 pseudocolor plots of the temperatures for the up- and downleg for 90 and 110 km are shown. In addition, velocity vectors are plotted to demonstrate the angle of attack and the flowfield magnitude.

From this figure, two effects, altitude and angle of attack, can be recognized as playing an important role in understanding the correction effects later in this paper. The flow becomes more rarefied as the altitude is increased. This is demonstrated by the much thicker shock layer in front of the rocket, which is proportional to the mean free path of the flow. During the upleg, the flow is directed downward, interacting more with the top of the rocket. This leads to a much smaller wake region compared with the downleg, where the flow is hitting the cylindrical shape of the rocket more from the side. This results in a much larger wake and shock in front of the rocket.

Figure 6 illustrates the inflow temperature $T_\infty$, obtained from the MSISE-00 model; the wall temperature of the rocket $T_{\text{wall}}$, obtained from temperature sensors on the rocket; and the maximum temperature $T_{\max}$, obtained from the simulations. The wall temperature stays below 400 K so that catalytic effects of the surface can be neglected. The maximum temperature in the flow is

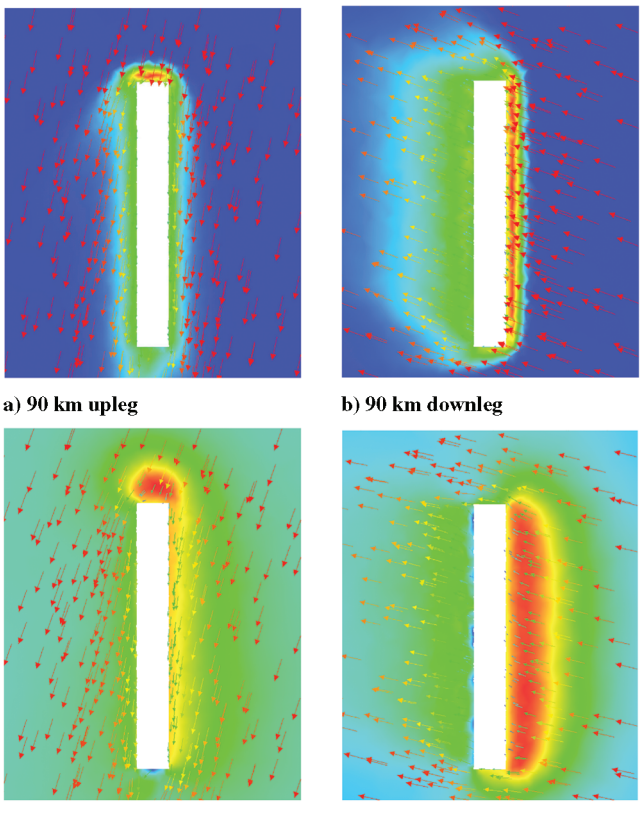

**a) 90 km upleg** **b) 90 km downleg**

**c) 100 km upleg** **d) 110 km downleg**

**Fig. 5 Steady-state up- and downleg temperature fields.**

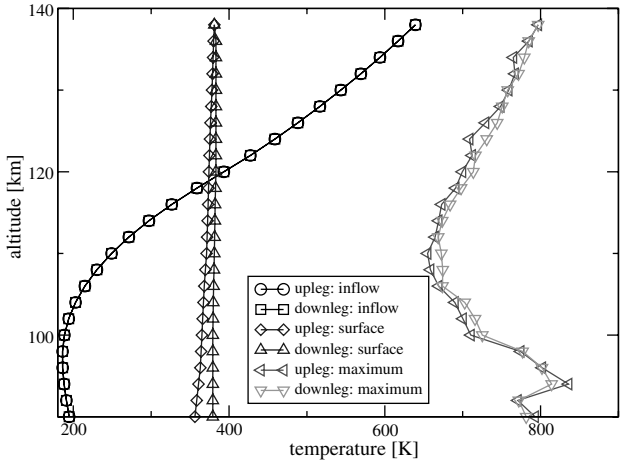


**Fig. 6 $T_\infty$, $T_{wall}$, and $T_{max}$ along the trajectory.**

around 835 K. These temperatures show that high temperature dissociation of $O_2$, as well as $N_2$ or $O_2$ vibrational excitation, have negligible influence in the considered cases.

### 3. *Number Density Fields*

Figure 7 shows contours of number density using foamDSMC for the upleg and downleg CODA II trajectory at the specified intervals shown. The most prominent feature at the lower altitudes (90 and 100 km) for both the upleg and downleg contours is the shock wave, which forms along the payload in accordance with the direction of the freestream velocity vector (indicated by the flow stream lines). The shock wave is clearly distinguished by the increased number density, which conveniently outlines the regions of ram and wake velocity orientations. This shock becomes much less defined as the altitude increases. As indicated from Table 1, the mean free path increases dramatically from 90 km to apogee, ranging from less than 2 cm to over 14 m. This increase in mean free path necessarily reduces the number of collisions between oncoming and reflected particles (particularly on the ram side), which otherwise would serve to create the characteristic shock appearance. The end result is a gradual increase in diffusivity and thickness of the shock until it is no longer distinguishable. The maximum density, as expected, occurs along the stagnation regions, which, for the majority of upleg cases, consists of the forward nose section of the payload. By contrast, this stagnation region for all of the downleg and certain upleg cases occurs along the entire ram side of the payload. The wake effect is also clearly visible and is distinguished in the contour plots by the dark blue hue. The concentration of particles in these regions can often be as much as 1 order of magnitude less than opposing concentrations within ram regions.

### 4. *Simulated Atomic Oxygen Concentration in the Sensor Field of View*

For each altitude simulated, the concentration of atomic oxygen was obtained at the location of the ATOX sensor field of view (see Fig. 1b). This was conducted for each of the three orientations and resulted in the upleg and downleg plots shown in Fig. 8. The maximum atomic oxygen concentration occurs near the 100 km altitude, and is in agreement with both the experimental data (see Figure 3) and the MSISE-00 [22] reference data. The magnitude of this maximum concentration, however, varies considerably between upleg and downleg values. The former (ram orientation) resulted in approximately 5.8E17 $m^{-3}$, whereas the latter had an approximate value of 1.2E18 $m^{-3}$. The reason for this significant jump in concentration between upleg and downleg (at equivalent altitudes) is due to the near-normal shock front, which occurs along much of the downleg trajectory, resulting from changes in angle of attack. Another consequence of the near-normal shock front along the downleg trajectory is the significant decrease in wake concentration, resulting in the "shadow" effect caused by the rocket payload.

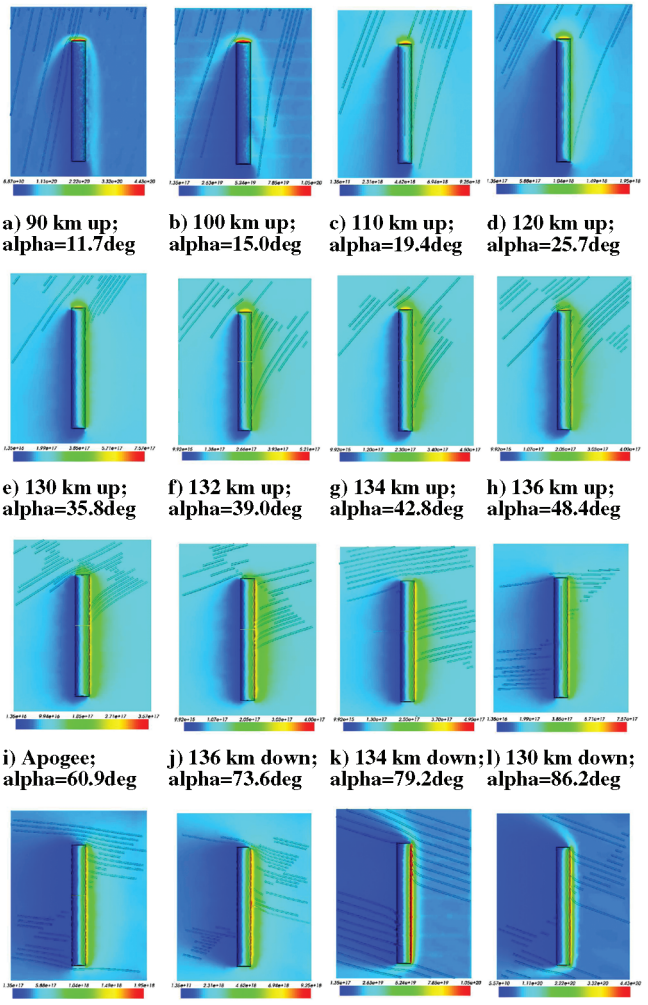


**Fig. 7 Steady-state upleg and downleg number density ($m^{-3}$) contours of CODA II at specified intervals, completed using the steady-state SMC solver.**

## B. Unsteady Results near Apogee

To study the effect of the unsteady change of the inflow conditions, the foamDSMC solver was used to simulate the unsteady flow of CODA II near its apogee. This altitude range was chosen, as mentioned previously, due to its relatively large mean free path ($\lambda_\infty = 14.01$ m) compared with lower altitudes. Similarly to the steady simulations, to maintain a statistically significant sample size, the average number of molecules per cell was no less than ten. This resulted in a computationally feasible study that allowed for relatively liberal cell sizes and time steps.

The unsteady flow was simulated along 10 m intervals beginning at 137 km upleg and ending at 137 km downleg. A 10 m interval was chosen because its length was less than the approximated mean free path ($\lambda_\infty = 14.01$ m, based on VHS model) and also because 10 m represented the refinement limit from which the MSISE-00 input data were taken. A total of 199 intervals were simulated up to and through apogee (138 km). Table 2 shows a small sampling of the unsteady input parameters used for the simulations.

The freestream flow and species properties in Table 2 were obtained from the MSISE-00 [22] atmospheric model, whereas the velocity and angles of attack were provided by the experiment. The largest variation over a single 10 m interval (0.1%) is due to increased flow rarefaction as quantified by the freestream number density. The relatively large $\lambda_\infty$ near apogee allowed for significantly larger cells than for steady simulations performed at lower altitudes (see, for comparison, Table 1). Figure 9 shows the number density profile

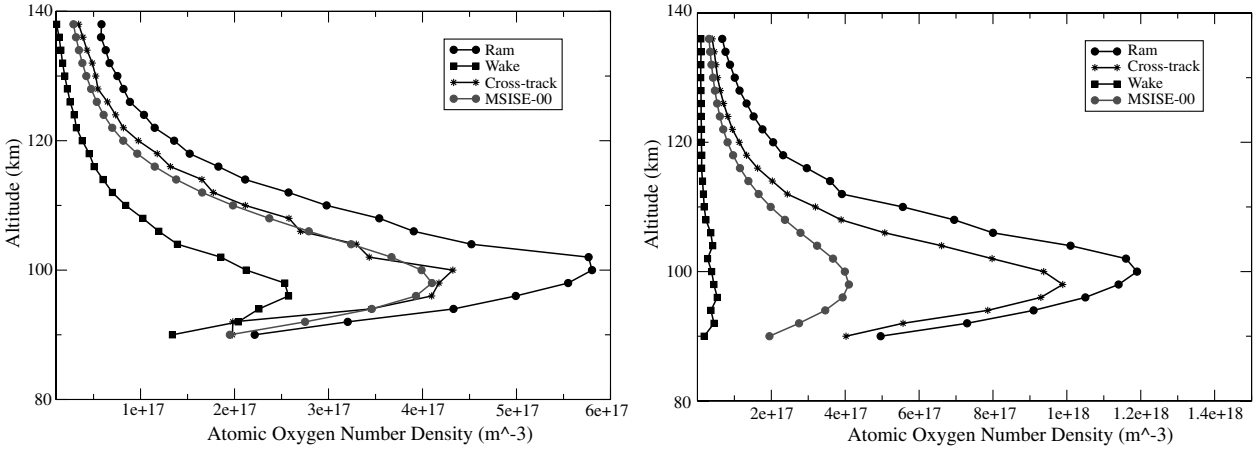


**a) Upleg** **b) Downleg**

**Fig. 8 Atomic oxygen number density ($m^{-3}$) along the upleg and downleg CODA II trajectory showing effect of ram, cross-track, and wake orientations. Also shown is the MSISE-00 [22] reference values of atomic oxygen.**

normal to the rocket through the sensor field of view using an increasing number of cells, and, because we keep the number of simulated molecules per cell constant, an increasing number of simulated molecules. With an average of 10 molecules per cell, the results indicate that cell refinement levels of 5.04E4 agree well with the much finer 9.67E4 level. The coarsest level, corresponding to 1.61E4, was deemed adequate, however, based on its relatively small deviation from the more refined cases at the locations of the ATOX sensor (see Fig. 9). Therefore, approximately 1.61E4 cells were employed, with an average of 2.0E5 multispecies, polyatomic molecules consisting of gaseous oxygen and nitrogen as well as atomic oxygen. Each interval was simulated using 20 independent ensembles, and the unsteady foamDSMC solver was run in parallel using eight processors over approximately a 20 h wall time period.

Figure 10 shows the unsteady results of the atomic oxygen number density in the sensor volume at/near apogee, corresponding to up and downleg atomic oxygen concentrations as a function of altitude. The values corresponding to ram, wake, and cross-track sensor orientations are shown, along with the MSISE-00 [22] reference values. Also shown are the steady-state results corresponding to 137.3 and 137.7 km for both the up- and downleg trajectories. As expected, the outlying atomic oxygen concentrations are seen from the ram and wake orientations, with average values of 5.75E16 $m^{-3}$ and 1.25E16 $m^{-3}$, respectively. The cross-track orientation shows the greatest tendency to follow the MSISE-00 trends. The cross-track and wake orientations maintain near constant values over the altitudes simulated, with the ram orientation showing the largest degree of time fluctuation. This fluctuation amounts to nearly 14% at its peak, and, although this fluctuation may likely be reduced with increased numbers of samples and/or ensembles, the data does conform to a clearly distinguishable mean value. Possibly the most important conclusion from these unsteady results is that the steady-state data lies within the uncertainty of the unsteady results. These findings effectively eliminate the need for unsteady simulations at these apogee/near-apogee altitudes, and, as suggested earlier, eliminate altogether the need for unsteady simulations over the entire trajectory.

## IV. Correction of Aerodynamic Effects

### A. Correction Factors

Following the approach of Rapp et al. [8], we define an aerodynamic correction factor (CF) as the ratio of freestream $n_\infty$ to measured $n$ concentrations:

$$\mathrm{CF} = \frac{n_\infty}{n} \tag{2}$$

Table 3 shows the computed atomic oxygen CF for each altitude simulated. The average upleg ram, cross-track, and wake corrections factors were computed as 0.66, 0.92, and 2.09, respectively, whereas the downleg results were 0.39, 0.62, and 7.84, respectively. As indicated, for both the upleg and downleg trajectories, the cross-track correction factor ($\mathrm{CF_{Cross}}$) shows the least disparity between disturbed and undisturbed concentrations. In particular, the upleg factor $\mathrm{CF_{Cross}}$ of 0.92 is merely 8% from a ratio of unity. In contrast, the wake correction factor $\mathrm{CF_{Wake}}$ shows the greatest degree of disunity, amounting to an average of 684% difference, along the downleg trajectory between concentrations of freestream and disturbed flow regions. This significant difference, particularly along the downleg trajectory, is due to the increasing alignment between the flowfield velocity vector and the direction of the sensor. The alignment of these vectors results in the creation of a near-normal shock wave, which greatly increases the amount of disequilibrium in the flow, particularly near the sensor field of view.

Figures 11 and 12 show the computed upleg and downleg, steady and unsteady correction factors as a function of altitude. The upleg,

**Table 2 A sampling of unsteady SMC input parameters**

| $H$, km | Frac. O | Frac. $O_2$ | Frac. $N_2$ | $n_\infty \times 10^{16}$ | $T$, K | $\alpha$, deg | $\lvert V\rvert$, m/s |
|---|---|---|---|---|---|---|---|
| 137.00 | 0.3059 | 0.0676 | 0.6264 | 9.78 | 628.3 | 52.44 | 842.56 |
| 137.01 | 0.3060 | 0.0676 | 0.6263 | 9.77 | 628.4 | 52.50 | 842.45 |
| ⋮ | ⋮ | ⋮ | ⋮ | ⋮ | ⋮ | ⋮ | ⋮ |
| 137.98 | 0.3110 | 0.0666 | 0.6224 | 9.21 | 639.1 | 60.91 | 833.300 |
| 137.99 | 0.3110 | 0.0665 | 0.6224 | 9.20 | 639.2 | 60.96 | 833.300 |
| **138.00** | **0.3110** | **0.0665** | **0.6224** | **9.20** | **639.3** | **61.00** | **833.300** |
| 137.99 | 0.3110 | 0.0665 | 0.6224 | 9.20 | 639.2 | 61.05 | 833.301 |
| 137.98 | 0.3110 | 0.0666 | 0.6224 | 9.21 | 639.1 | 61.10 | 833.303 |
| ⋮ | ⋮ | ⋮ | ⋮ | ⋮ | ⋮ | ⋮ | ⋮ |
| 137.01 | 0.3060 | 0.0676 | 0.6263 | 9.77 | 628.4 | 69.60 | 842.9 |
| 137.00 | 0.3059 | 0.0676 | 0.6264 | 9.78 | 628.3 | 69.66 | 843.02 |

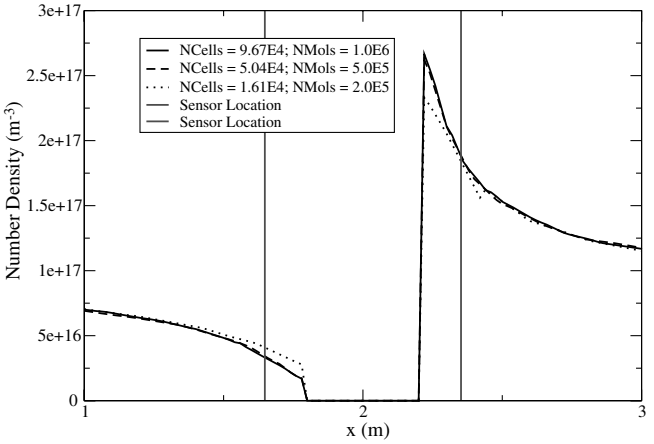


**Fig. 9 Grid convergence study near apogee.**

steady-state plot (upper left) of Fig. 11 shows two large spikes occurring for both the ram and cross-track orientations located at approximately 102 and 92 km, respectively. These spikes occur when the sensor volume is within the shock region and small changes in location can results in relativeley large changes in the number density. Additional, exploded views of the unsteady results are also presented near apogee. Unlike the upleg, the downleg, cross-track correction factor, shown in Fig. 12 is significantly less than unity, particularly at the lower altitudes.

The large differences between the upleg and downleg correction factors resulted from the large changes of angle of attack. As seen in Fig. 5, the flow in the upleg comes from the top region of the rocket and shows a totally different flowfield compared with the downleg, where the flow comes more from the side of the rocket.

### B. Corrected Atomic Oxygen Data

Figure 13a shows the normalized concentration of atomic oxygen along the upleg trajectory, comparing corrected and uncorrected values between the ram and cross-track orientations. Unfortunately, the wake experimental data was incomplete, and was, therefore, not included for correction. As indicated, the corrected ram and cross-track data appear nearly as one continuous curve. This is in stark contrast to their respective uncorrected data sets. This nearly complete convolution of ram and cross-track data suggests that the effect due to compressible flow aerodynamics accounts for the bulk of the upleg orientation differences. It further suggests that the use of correction factors obtained from DSMC numerical simulations represents a viable option to substantially minimize these unwanted effects and arrive at closer approximations to actual freestream conditions.

**Table 3 Atomic oxygen correction factors for ram, cross-track, and wake ATOX sensor orientations**

| $H$, km | $CF_{Ram}$ up/down | $CF_{Cross}$ up/down | $CF_{Wake}$ up/down |
|---|---|---|---|
| 90 | 0.88/0.39 | 0.99/0.48 | 1.46/10.67 |
| 92 | 0.86/0.38 | 1.39/0.49 | 1.35/6.11 |
| 94 | 0.80/0.38 | 1.00/0.44 | 1.53/9.45 |
| 96 | 0.79/0.37 | 0.96/0.42 | 1.53/7.32 |
| 98 | 0.74/0.36 | 0.98/0.41 | 1.62/9.20 |
| 100 | 0.69/0.34 | 0.92/0.43 | 1.88/10.36 |
| 102 | 0.64/0.32 | 1.07/0.46 | 1.98/13.4 |
| 104 | 0.93/0.32 | 0.98/0.49 | 2.33/7.84 |
| 106 | 0.71/0.35 | 1.03/0.55 | 2.34/7.72 |
| 108 | 0.67/0.34 | 0.92/0.61 | 2.31/10.28 |
| 110 | 0.67/0.36 | 0.94/0.62 | 2.36/10.83 |
| 112 | 0.64/0.42 | 0.93/0.68 | 2.36/10.15 |
| 114 | 0.65/0.38 | 0.83/0.68 | 2.3/10.05 |
| 116 | 0.63/0.39 | 0.87/0.71 | 2.28/10.24 |
| 118 | 0.63/0.42 | 0.82/0.73 | 2.13/8.18 |
| 120 | 0.60/0.40 | 0.83/0.72 | 2.15/7.64 |
| 122 | 0.61/0.40 | 0.85/0.74 | 2.20/6.37 |
| 124 | 0.59/0.40 | 0.83/0.74 | 2.06/6.11 |
| 126 | 0.60/0.40 | 0.82/0.75 | 2.13/5.36 |
| 128 | 0.58/0.42 | 0.87/0.77 | 2.14/4.93 |
| 130 | 0.56/0.42 | 0.81/0.78 | 2.19/4.80 |
| 132 | 0.57/0.43 | 0.78/0.76 | 2.23/4.16 |
| 134 | 0.55/0.45 | 0.80/0.76 | 2.26/3.50 |
| 136 | 0.54/0.47 | 0.81/0.78 | 2.34/3.39 |
| 138 | 0.49 | 0.84 | 2.68 |

Figure 13b shows the normalized concentration of atomic oxygen along the downleg trajectory, again comparing corrected and uncorrected values between the ram and cross-track orientations. As indicated, the agreement between corrected ram and cross-track concentration data is quite good up until approximately 100 km altitude. Upwards of 100 km, the agreement declines somewhat and amounts to a variation of approximately 18% at 110 km. Compared with the significant variation of uncorrected ram and cross-track concentration values, however, the corrected values still represent a significant improvement. The disparity is likely the result of additional external factors, such as contamination of sensor optics through desorption or outgassing or, potentially, chemical reactions of desorbed water vapor with atmospheric atomic oxygen. The effects of some of these additional external factors will be considered in future studies.

The biggest contributing factor to the difference between the corrected atomic oxygen density and the MISISE-00 can be explained through the mission goals of the CODA II experiment. CODA II was launched to observe the effects of an active aurora on the neutral atmosphere. Periods of increased auroral activity serve to

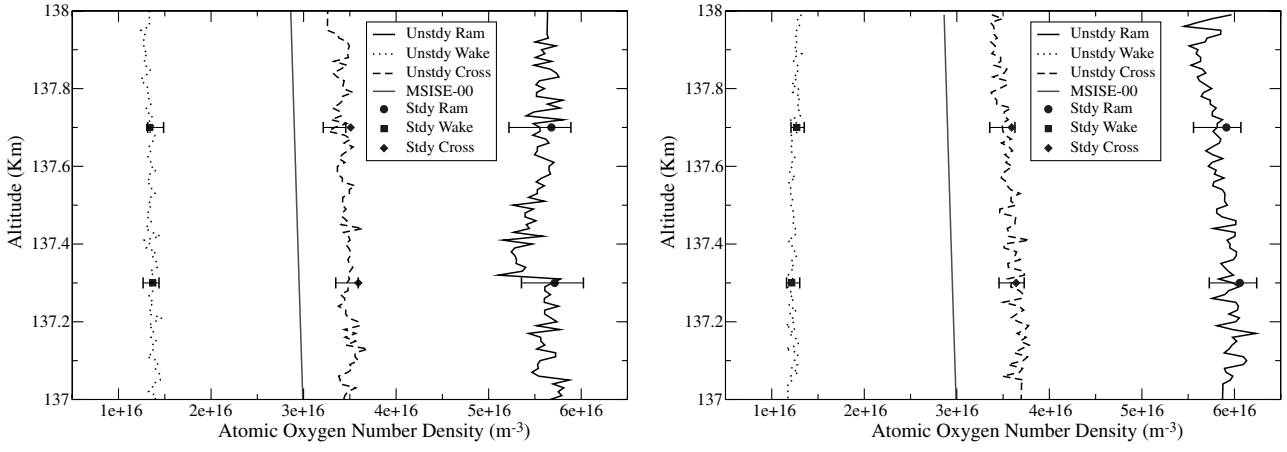


**a) Upleg** **b) Downleg**

**Fig. 10 Unsteady and selected steady-state atomic oxygen concentrations in the ATOX sensor field of view using SMC, showing results from ram, wake, cross-track, and MSISE-00 data [22] at/near apogee.**

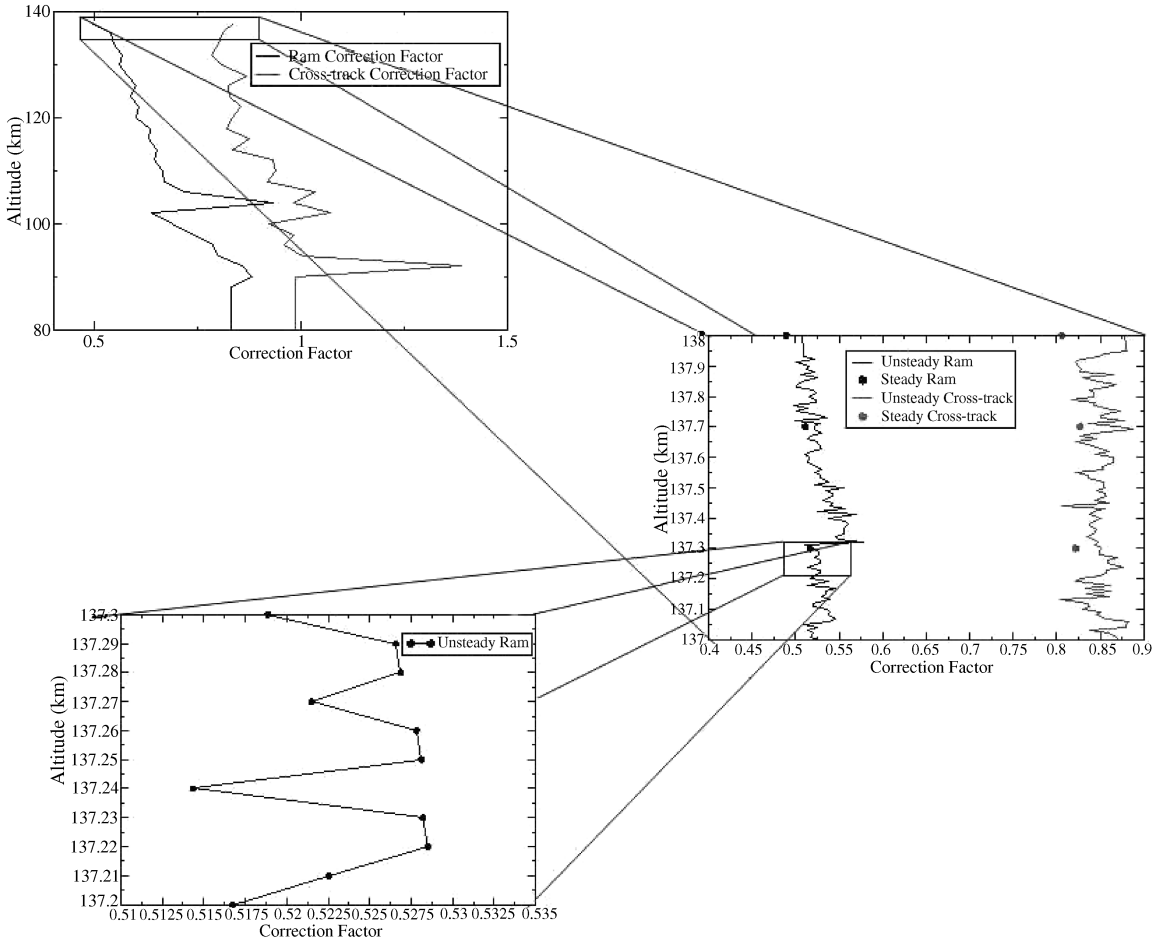


**Fig. 11 Upleg steady and unsteady ram/cross-track correction factors as functions of altitude.**

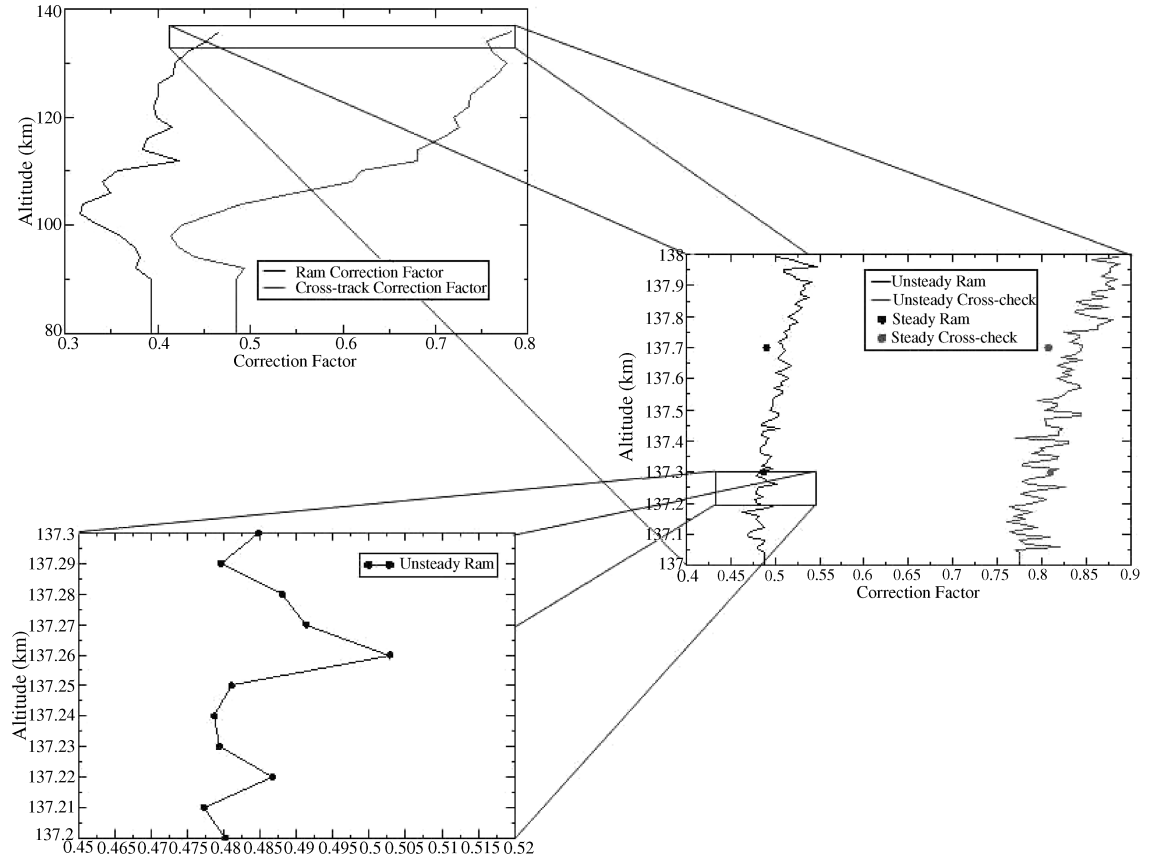


**Fig. 12 Downleg steady and unsteady ram/cross-track correction factors as functions of altitude.**

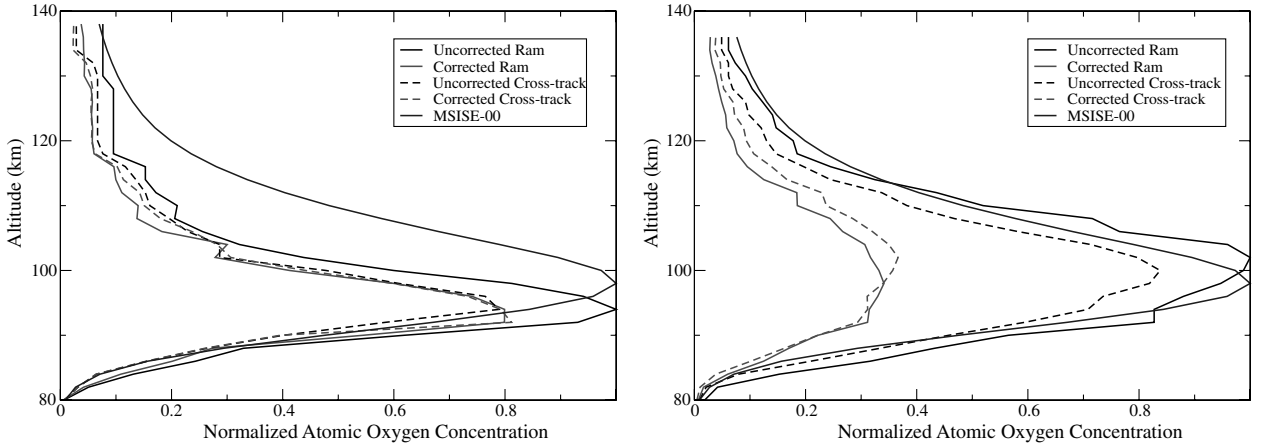


**Fig. 13 Normalized atomic oxygen concentration data along the upleg trajectory. The results include uncorrected, corrected, and MSISE-00 [22] data.**

increase levels of atomic oxygen through the dissociation of $O_2$ ("Auroral $O_2$ dissociation").

## V. Conclusions

This research was conducted to better quantify the freestream atomic oxygen concentration within the Earth's upper atmosphere. A new, parallel, steady/unsteady DSMC solver, foamDSMC, was applied to numerically solve for the flowfield surrounding the atomic oxygen sensors pertaining to the CODA II sounding rocket. The steady-state results clearly showed the significant influence of the compressible flow aerodynamics on atomic oxygen concentration measurements. The unsteady results revealed that the unsteady data lay well within the steady-state data and, thus, substantiated the adequacy of the steady-state simulations for the whole trajectory. The steady-state results prompted the creation of correction functions based on the ratio of freestream to disturbed concentrations. The resulting correction functions, when applied to the experimentally derived CODA II data sets, showed a significant minimization of the flowfield aerodynamic effect, particularly along the upleg trajectory. The three-dimensional results presented here are also applicable to other side-looking instruments, which suffer from the aerodynamic effects of the sounding rocket flowfield. Also, with the parallel computing techniques used in this study, simulations like this can become routine to improve the data from side-looking sounding rocket instruments. Our simulations could be performed using about 100 processors on a Linux cluster supercomputer within 24 h using a combination of job level and solver level parallelism. This makes the high-resolution correction of those sensor data feasible for other sounding rocket experiments with side-looking instruments.

In future studies, the authors wish to investigate additional external effects, including the possibility of sensor contamination from desorption and outgassing of water vapor from the payload surfaces. Additionally, possible chemical reactions occurring between the water vapor and atmospheric atomic oxygen may play a significant role in altering atomic oxygen concentrations.

## Acknowledgments

The computational resource, the Uinta cluster supercomputer, was provided through the National Science Foundation under grant no. CTS-0321170 with matching funds provided by Utah State University. The authors would like to primarily acknowledge the Space Dynamics Laboratory and the enabling technologies program. Computer time from the Center for High Performance Computing at Utah State University is gratefully acknowledged.

## References

[1] Gumbel, J., "A Review of Direct Atomic Oxygen Measurements in the Mesosphere and Lower Thermosphere," *AGU Fall Meeting*, American Geophysical Union, Washington, D.C., 1999.

[2] Patterson, P., "In Situ Measurements of Upper Atmospheric Atomic Oxygen: The ATOX Resonant Fluorescence/Absorption Sensor," Ph.D. Thesis, Utah State Univ., Logan, UT, 2005.

[3] Bird, G. A., "Aerodynamic Effects on Atmospheric Composition Measurements from Rocket Vehicles in the Thermosphere," *Planetary and Space Science*, Vol. 36, Sept. 1988, pp. 921–926. doi:10.1016/0032-0633(88)90099-2

[4] Gumbel, J., Murtagh, D., Espy, P., Witt, G., and Schmidlin, F., "Odd Oxygen Measurements During the Noctilucent Cloud 93 Rocket Campaign," *Journal of Geophysical Research*, Vol. 103, No. A10, 1998, pp. 23399–23414. doi:10.1029/98JA02155

[5] Horanyi, M., Gumbel, J.,Witt, G., and Robertson, S., "Simulation of Rocket-Borne Particle Measurements in the Mesosphere," *Geophysical Research Letters*, Vol. 26, No. 11, 1999, pp. 1537–1540. doi:10.1029/1999GL900298

[6] Gumbel, J., "Rarefied Gas Flows Through Meshes and Implications for Atmospheric Measurements," *Annales Geophysicae*, Vol. 19, No. 5, 2001, pp. 563–569.

[7] Kurihara, J., Oyama, K., Iwagami, N., and Takahashi, T., "Numerical Simulation of 3-D Flow Around Sounding Rocket in the Lower Thermosphere," *Annales Geophysicae*, Vol. 24, No. 1, 2006, pp. 89–95.

[8] Rapp, M., Gumbel, J., and Lübken, F., "Absolute Density Measurements in the Middle Atmosphere," *Annales Geophysicae*, Vol. 19, No. 5, 2001, pp. 571–580.

[9] Allen, J., Perl, M., and Hauser, T., "Aerodynamic Influences on Atomic Oxygen Sensors from Sounding Rockets," *Journal of Spacecraft and Rockets*, Vol. 43, No. 6, 2006, pp. 1387–1394. doi:10.2514/1.19060

[10] Allen, J., and Hauser, T., "foamDSMC: An Object Oriented Parallel DSMC Solver for Rarefied Flow Applications," *45th AIAA Aerospace Sciences Meeting and Exhibit*, AIAA, Reston, VA, Jan. 2007, pp. 1106–1120.

[11] Xavier, C., and Iyengar, S., *Introduction to Parallel Algorithms*, Wiley, New York, 1998.

[12] Dietrich, S., and Boyd, I., "Scalar and Parallel Optimized Implementation of the Direct Simulation Monte Carlo Method," *Journal of Computational Physics*, Vol. 126, No. 2, 1996, pp. 328–342. doi:10.1006/jcph.1996.0141

[13] Gumbel, J., "Aerodynamic Influences on Atmospheric In Situ Measurements from Sounding Rockets," *Journal of Geophysical Research*, Vol. 106, No. A6, 2001, pp. 10,553–10,563. doi:10.1029/2000JA900166

[14] Ridley, B., Davenport, J., Stief, L., and Welge, K., "Resonance Line Broadening in Helium Discharge Lamps," *Journal of Chemical Physics*, Vol. 57, No. 1, July 1972, pp. 520–530. doi:10.1063/1.1677994

[15] Patterson, P., Swenson, C., Clemmons, J., Christensen, A., and Gregory, J., "Atomic Oxygen Erosion Observations in a Diffuse Aurora," AGU Fall Meeting, American Geophysical Union, Paper SA21A-02, Dec. 2003.

[16] Sun, Q., Boyd, I., Cai, C., Clemmons, J., and Hecht, J., "Computational Analysis of High-Altitude Ionization Gauge Flight Measurements," *Journal of Spacecraft and Rockets*, Vol. 43, No. 1, 2006, pp. 186–193.

[17] Zuber, A., "Resonance Light Sources and Their Use in Atmospheric Research," Ph.D. Thesis, Univ. of Stockholm, Stockholm, 1989.
[18] Bird, G., *Molecular Gas Dynamics and the Direct Simulation of Gas Flows*, Oxford Univ. Press, Sydney, Australia, 1994.
[19] Nanbu, K., "Theoretical Basis of the Direct Simulation Monte Carlo Method," *15th International Symposium on Rarefied Gas Dynamics*, B. G. Tuebner, Stuttgart, Germany, 1986, pp. 369–383.
[20] Wagner, W., "A Convergence Proof for Bird's Direct Simulation Monte Carlo Method for the Boltzmann Equation," *Journal of Statistical Physics*, Vol. 66, Nos. 3–4, 1992, pp. 1011–1044. doi:10.1007/BF01055714
[21] Oran, E., Oh, C., and Cybyk, B., "Direct Simulation Monte Carlo: Recent Advances and Applications," *Annual Review of Fluid Mechanics*, Vol. 30, No. 1, Jan. 1998, pp. 403–441. doi:10.1146/annurev.fluid.30.1.403
[22] Hedin, A., "Extension of the MSIS Thermospheric Model into the Middle and Lower Atmosphere," *Journal of Geophysical Research*, Vol. 96, No. A2, 1991, pp. 1159–1172. doi:10.1029/90JA02125
[23] Weller, H., Tabor, G., Jasak, H., and Fureby, C., "A Tensorial Approach to Computational Continuum Mechanics Using Object Orientated Techniques," *Computers in Physics*, Vol. 12, No. 6, 1998, pp. 620–631.

I. Boyd
*Associate Editor*